Scripta Materialia 158 (2019) 50–56

Contents lists available at ScienceDirect

Scripta Materialia

journal homepage: www.elsevier.com/locate/scriptamat

Phase transformations of HfNbTaTiZr high-entropy alloy at intermediate temperatures☆

S.Y. Chen [a], Y. Tong [a], K.-K. Tseng [b], J.-W. Yeh [b], J.D. Poplawsky [c], J.G. Wen [d], M.C. Gao [e,f], G. Kim [g], W. Chen [g], Y. Ren [h], R. Feng [a], W.D. Li [a], P.K. Liaw [a,*]

[a] Department of Materials Science and Engineering, The University of Tennessee, Knoxville, TN 37996, USA
[b] High Entropy Materials Center, Department of Materials Science and Engineering, National Tsing Hua University, Hsinchu 30013, Taiwan
[c] Center for Nanophases Materials Sciences, Oak Ridge National Laboratory, Oak Ridge, TN 37831, USA
[d] Center for Nanoscale Materials, Argonne National Laboratory, Argonne, IL 60439, USA
[e] National Energy Technology Laboratory, Albany, OR 97321, USA
[f] AECOM, P.O. Box 618, South Park, PA 15129, USA
[g] Department of Mechanical, Materials and Aerospace Engineering, Illinois Institute of Technology, Chicago, IL 60616, USA
[h] X-ray Science Division, Argonne National Laboratory, Argonne, IL 60439, USA

ARTICLE INFO

Article history:
Received 10 July 2018
Received in revised form 14 August 2018
Accepted 17 August 2018
Available online 28 August 2018

Keywords:
High-entropy alloys
Phase decomposition
Annealing

ABSTRACT

The strong and ductile single-phase body-centered-cubic (BCC) HfNbTaTiZr refractory high-entropy alloy (RHEA) is a potential structural material for high-temperature applications. However, the BCC phase stability in the intermediate temperature range (500–900 °C) needs to be better understood to make this alloy applicable to industry. In the present work, the phase decomposition of the HfNbTaTiZr RHEA is examined at different temperatures (500–1000 °C). Additionally, the formation of BCC Ta-Nb-rich and hexagonal-close-packed (HCP) Hf-Zr-rich precipitates are studied as a function of annealing time at 700 °C using a combination of atom probe tomography, transmission electron microscopy, and X-ray diffraction. We found that these BCC and HCP precipitates have preferred orientations with the BCC matrix.

Refractory high-entropy alloys (RHEAs) have motivated rapidly increasing investigations due to their exceptional high-temperature mechanical properties and great application potential in thermally-harsh environments (e.g., aerospace and power-generation industries) [1–9]. However, a key bottleneck that hinders their real-world applications is the brittleness and poor malleability at low temperatures. It was recently reported that the HfNbTaTiZr RHEA could overcome this hurdle by exhibiting a combination of high strength and good ductility [6,9]. To promote applications of this alloy at elevated temperatures, maintaining the high phase stability in a broad temperature range during a prolonged service time is crucial to retain its stable structural performance.

The HfNbTaTiZr RHEA in the as-cast state as well as after annealing above ~1000 °C [6,9–12] is generally regarded as a single-phase body-centered-cubic (BCC) solid solution with high stability because of a large contribution of the configurational entropy to the Gibbs free energy. However, contrary to the commonly-expected high-entropy effect that should stabilize the BCC phase at high temperatures, recent investigations by Senkov et al. [9,10] demonstrated that two BCC phases corresponding to Nb-Ta-rich precipitate and Hf-Zr-rich matrix were formed after annealing a cold-rolled HfNbTaTiZr RHEA at 800 °C for 2 h. Furthermore, they found that the diffusion of Nb and Ta may control the precipitate coarsening in the HfNbTaTiZr at 800 °C, due to their low self-diffusivities and interdiffusion, compared with that of Ti and Zr [10]. Controversy also exists for the phase stability of the HfNbTaTiZr RHEA at intermediate temperatures of 500–900 °C. For example, Stepanov et al. [11] reported the formation of two phases with hexagonal-closed-packed (HCP) and BCC structures after annealing a homogenized HfNbTaTiZr at 800 °C for 100 h. Schuh et al. [12] recently examined the stability of the nanocrystalline HfNbTaTiZr RHEA and reported the formation of three phases (two BCC and one HCP phases) after annealing at 800 °C for 1 h or at 500 °C for 100 h. Moreover, calculated phase diagram (Calphad) simulation results suggest that the single phase at high temperatures starts to decompose into three phases when the temperature is below 800 °C, which is in agreement with the

☆ This manuscript has been authored by UT-Battelle, LLC under Contract No. DE-AC05-00OR22725 with the U.S. Department of Energy. The United States Government retains and the publisher, by accepting the article for publication, acknowledges that the United States Government retains a non-exclusive, paid-up, irrevocable, world-wide license to publish or reproduce the published form of this manuscript, or allow others to do so, for United States Government purposes. The Department of Energy will provide public access to these results of federally sponsored research in accordance with the DOE Public Access Plan (http://energy.gov/downloads/doe-public-access-plan).

* Corresponding author.
E-mail address: pliaw@utk.edu (P.K. Liaw).

https://doi.org/10.1016/j.scriptamat.2018.08.032
1359-6462/

experimental results found in the nanocrystalline HfNbTaTiZr RHEA [12]. Compared with the bulk form, precipitation behavior in the nanocrystalline alloys, however, may behave differently under annealing due to a high fraction of grain boundaries acting as heterogeneous nucleation sites. Aimed to clarify above controversy, the microstructural evolution of the bulk HfNbTaTiZr alloy in the intermediate temperature range was detailed in the present study.

The HfNbTaTiZr buttons were prepared by arc-melting in an argon atmosphere. The solidified buttons were cut into slabs with dimensions of 13.5 mm × 25 mm × 50 mm, and then cold-rolled to a final thickness of 4 mm (a total reduction of ~70%) with the imposed per-pass thickness reduction of 0.25 mm. The rolled sheets were then sealed in vacuum-quartz tubes and then homogenized at 1200 °C for 10 min., followed by water quenching. The as-homogenized alloys were subsequently annealed at (550–1000 °C) for 96 h or at 700 °C for 2.5 h, 96 h, and 192 h, respectively.

The crystal structures of the heat-treated samples were examined by synchrotron X-ray diffraction (XRD) with an energy of 111 keV (λ = 0.1173 Å) at the ID-11 Advanced Photon Sources (APS), Argonne National Laboratory (ANL). The diffraction data were collected with a two-dimensional (2D) detector, which was placed about 1200 mm behind the sample. The 2D diffraction data were processed with the Fit2D software [13]. Besides, the crystal structures of annealed samples were identified by a Panalytical Empyrean X-ray diffractometer with Cu Kα radiation as well. To further investigate the microstructure evolution, several advanced characterization methods were employed, including scanning electron microscopy (SEM) operated in a back-scattered electron (BSE) mode, transmission electron microscopy (TEM) with energy-dispersive X-ray spectroscopy (EDS), and atom probe tomography (APT). The standard bright-field images and selected area diffraction patterns were obtained, using a FEI Talos F200X and the Argonne Chromatic Aberration-corrected TEM (ACAT) at ANL, respectively. An FEI Nova 200 dual-beam focused ion beam (FIB) instrument was used to perform site-specific lift-outs of specimen regions-of-interest (ROI) and annular milling to fabricate the needle-shaped APT specimens. The APT measurements were performed with a CAMECA Instruments LEAP 4000X HR in a laser mode with a 50 pJ pulse energy at 30 K and a detection rate of 0.005 atoms per pulse. The collected dataset was reconstructed by the CAMECA IVAS 3.8 software [14,15].

Fig. 1(a) shows that the homogenized specimen has the typical recrystallization microstructure with equiaxed-grains. The corresponding EDS mapping in Fig. 1(b–f) reveals a homogeneous distribution of the composition in the as-homogenized sample. The phase of the homogenized specimen was verified by the synchrotron XRD measurement, shown in Fig. 2(a). The homogenized sample has a single BCC phase with a lattice constant of 3.408 Å. Fig. 2(a) also presents the synchrotron XRD patterns of the specimens annealed at 550, 700, 900, and 1000 °C for 96 h. For the sample annealed at 1000 °C, only a single BCC phase was found. When annealed at 900 °C, the BCC phase becomes unstable by showing peak splitting. Multiple phases were observed at 550 and 700 °C, which were confirmed as two BCC phases and one HCP phase, consistent with the previous phase diagram calculation results [12]. Specifically, several minor peaks were corresponding to the BCC matrix disappear when the specimen annealed at 550 °C, compared with that at 700 °C. The phases present after annealing experiments at various temperatures are summarized in Table 1. Fig. 2(b) shows the synchrotron XRD patterns of specimens annealed at the specific temperature of 700 °C for 2.5 h, 96 h, and 192 h. The specimen annealed at 700 °C for 2.5 h has a major BCC phase and another minor BCC phase (confirmed as the Ta-Nb-rich BCC phase later). After annealing at 700 °C for 96 and 192 h, three phases are formed, identified as two major BCC phases and one minor HCP phase. The two BCC phases have a lattice parameter of 3.447 Å (denoted as BCC1) and 3.323 Å (denoted as BCC2), respectively. The lattice parameters of the HCP phase are: a = 3.143 Å and c = 5.042 Å. The microstructures of the samples annealed at 700 °C for 2.5, 96, and 192 h were shown in Fig. 2(c–h). After the short annealing time of 2.5 h, precipitates with an irregular morphology formed along the grain boundaries, with the volume fraction of about 3.23%. After annealing at 700 °C for 96 h [Fig. 2(e, f)], precipitates with a lamellar shape were formed along grain boundaries, and meanwhile round-shape precipitates were developed within grains, with increasing the total volume fraction of about 41.2%. With increasing the annealing time to 192 h [Fig. 2(g, h)], precipitate coarsening occurs within the grains, while a morphology change of the precipitates at grain boundaries from the lamellar to spherical shapes occurs due to a reduction of the total interface energy. The total volume fraction of precipitates is about 39.8%.

Fig. 3(a–g) shows a bright-field (BF) scanning transmission electron microscopy (STEM) image of the sample annealed at 700 °C for 96 h and its corresponding elemental-distribution maps obtained by STEM-EDS. The TEM image of the microstructure is taken from a grain interior containing precipitates. Consistent with the XRD results, the elemental maps reveal three phases: the Ta-Nb-rich phase found in the area denoted as N1 in Fig. 3(a) and (g), the Hf-Zr-rich phase indicated as the N2 area, and the phase with almost evenly-distributed elements in the area denoted as N3. The compositions of the three multi-element

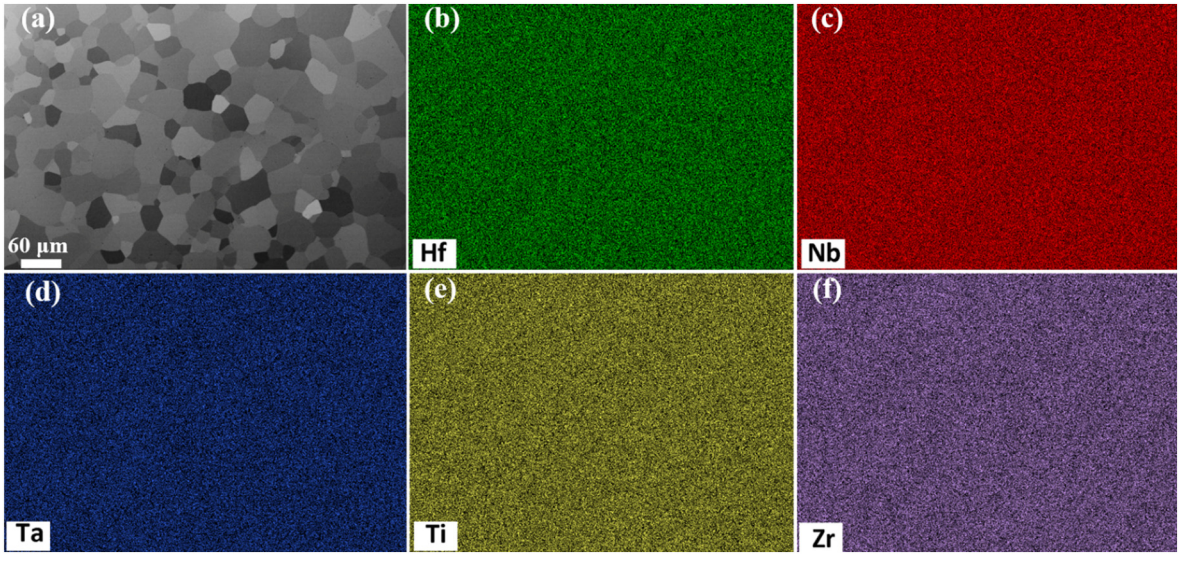

Fig. 1. SEM image (a) and the corresponding EDX maps (b–f) of as-homogenized specimen.

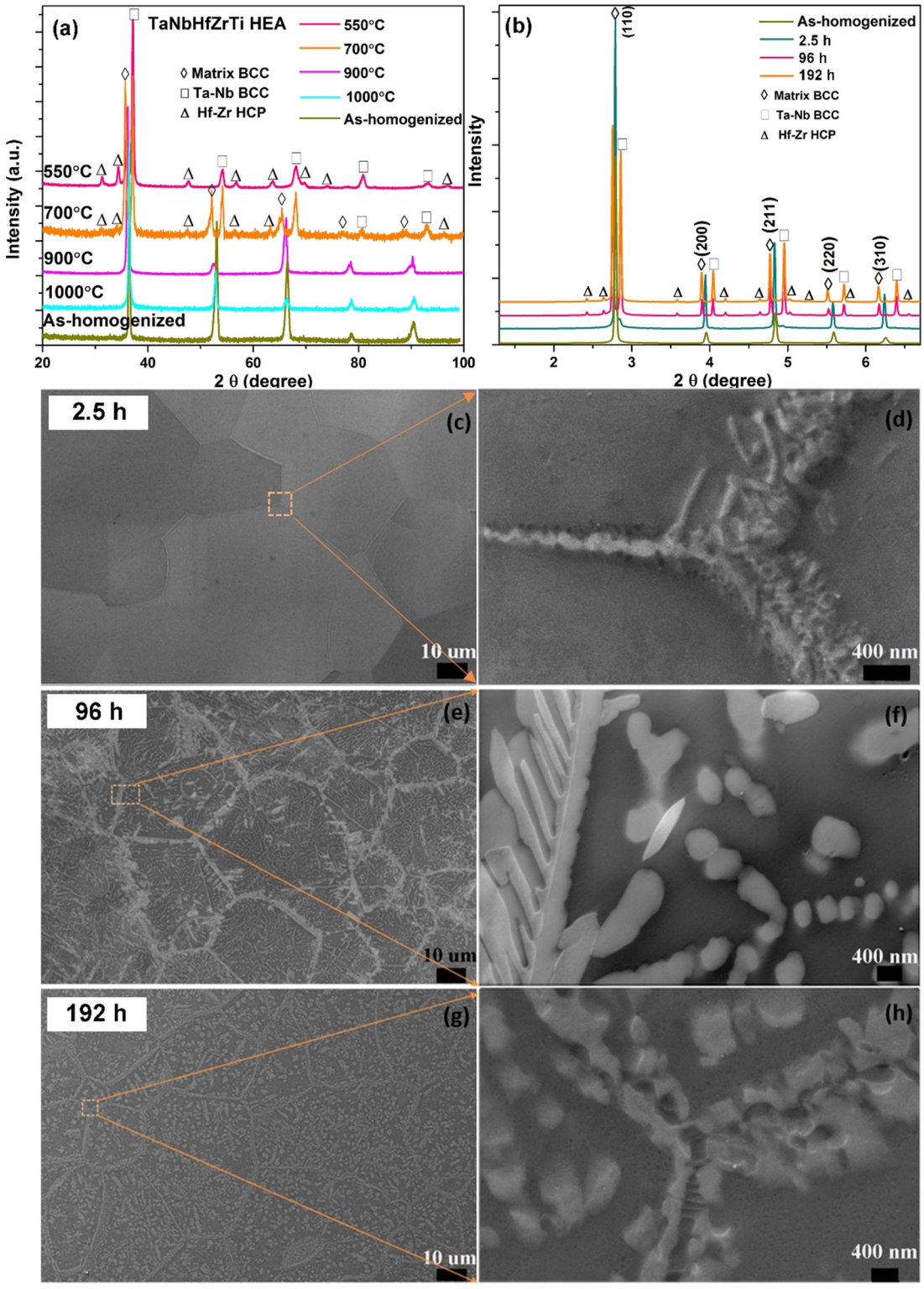

Fig. 2. Synchrotron XRD patterns of specimens annealed at different temperatures for 96 h (a) and annealed at the temperature of 700 °C for 2.5 h, 96, and 192 h (b). The synchrotron XRD pattern from the as-homogenized sample is also included; (c–h) SEM images of specimens annealed at 700 °C for 2.5 h (c, d), 96 h (e, f) and 192 h (g, h).

phases based on the TEM-EDS analysis are summarized in the "TEM" row of Table 2. The SEM-EDS analysis (not shown) is unable to reveal the compositional difference due to the phase size being smaller than 1 μm. Fig. 3(h–k) shows the APT atom maps and proximity histograms of the Ta-Nb-rich and Hf-Zr-rich phases. For the sample annealed at 700 °C for 2.5 h, the XRD result suggests a major BCC phase with a small amount of Ta-Nb-rich and Hf-Zr-rich precipitates, which was observed in the compositional analysis by APT [Fig. 3(h)]. The sample annealed at 700 °C for 96 h presents three phases with different elemental compositions, which was further characterized by APT as well [Fig. 3(i)]. The tip sample was taken from the grain-boundary (GB) region. The analyzed APT area was close to a GB. The elemental-concentration profiles generated from an iso-concentration surface (proximity histograms) between the Ta-Nb-rich and Hf-Zr-rich precipitates presented

Table 1
The phase formation in samples annealed in the temperature range of 550–1000 °C.

Temperatures (°C)	550	700	900	1000	As-homogenized
Phases	TaNb BCC + minor matrix BCC + HfZr HCP	TaNb BCC + matrix BCC + HfZr HCP	Minor TaNb BCC + matrix BCC	Matrix BCC	Matrix BCC

in Fig. 3(h, i) are exhibited in Fig. 3(j, k). The compositional analysis of the sample annealed for 96 h is listed as the "APT" row in Table 2. It should be noticed that there are some compositional differences for the Ta-Nb-rich and Hf-Zr-rich phases between TEM-EDS and APT results, which might be due to the inherent composition difference from solidification at grain boundaries and grain interiors. This trend does not influence the phase transformation in the present study. The corresponding compositions for each phase obtained from APT are summarized in Table 2 as well.

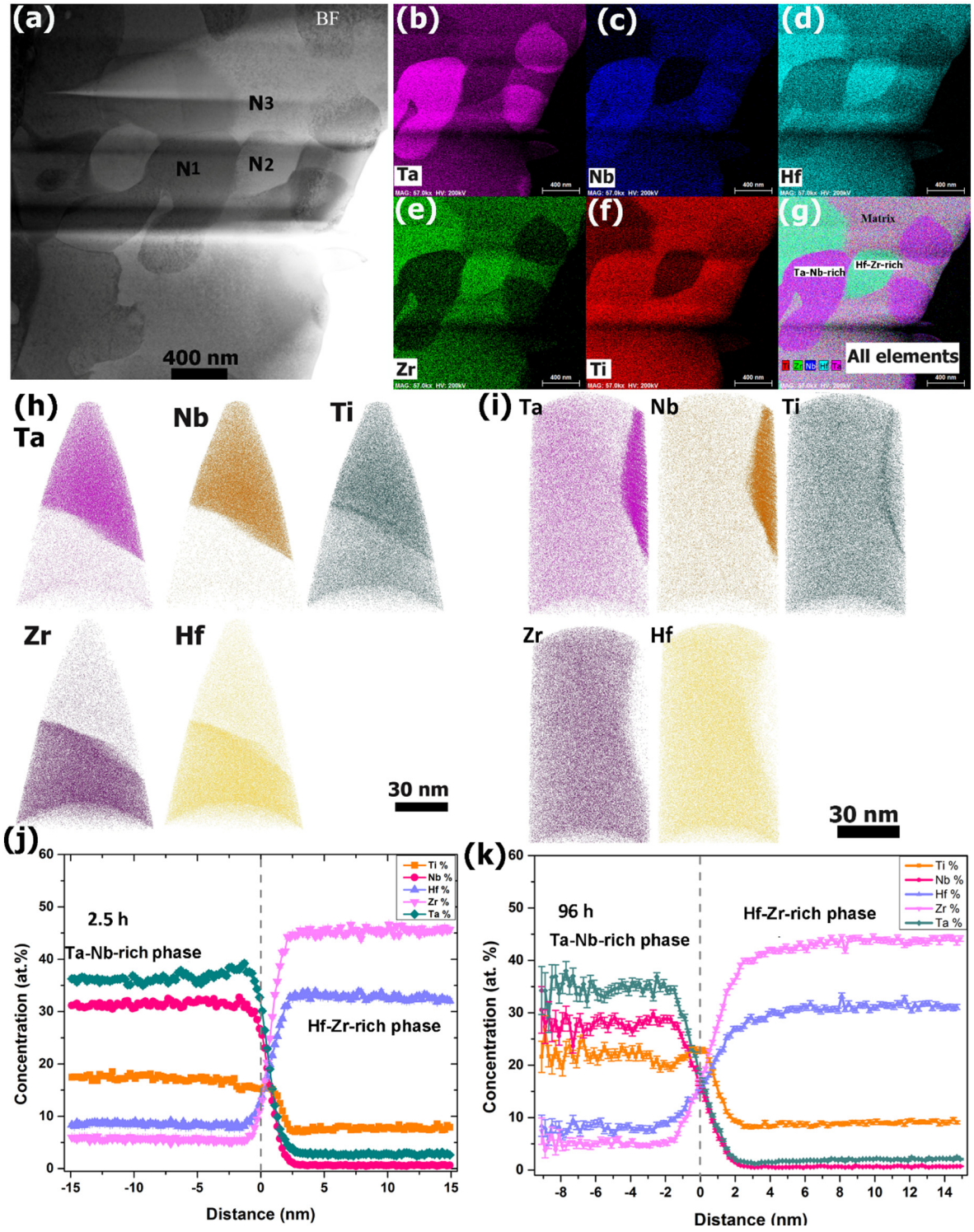

Fig. 3. (a) Bright-field (BF) TEM image of the specimen after aging at 700 °C for 96 h; the corresponding elemental-distribution maps (b–f) and overall map (g) obtained by STEM-EDS; atom maps of samples annealed for 2.5 h (h) and 96 h (i) reconstructed from the APT analysis; proximity histograms of concentration profiles of samples annealed for 2.5 h (j) and 96 h (k).

Table 2
The compositions of each phase in the sample annealed at 700 °C for 96 h.

Phase		Ta (at.%)	Nb (at.%)	Ti (at.%)	Zr (at.%)	Hf (at.%)
Ta-Nb-rich BCC	TEM-EDX	42.81	29.67	15.27	5.32	6.93
	APT	38.52	33.44	17.46	4.05	6.53
	CALPHAD	40.95	40.57	12.22	3.54	2.73
Hf-Zr-rich HCP	TEM-EDX	7.62	0.75	10.43	43.99	37.21
	APT	5.87	0.39	9.31	49.04	35.39
	CALPHAD	0.57	0.92	27.21	35.27	36.02
Matrix BCC	TEM-EDX	21.10	13.37	22.09	20.28	23.16
	APT	20.53	21.10	20.10	19.50	18.77

Note.
TEM-EDX: data was collected in the grain interior; APT: data was collected at the location close to the grain boundary.

Selected area electron diffraction (SAED) was performed to obtain the information regarding the crystal structure of each phase in Fig. 3 (a). Fig. 4(a) and (b) shows the SAED patterns of N1 together with the matrix, N3. Both the Ta-Nb-rich phase (N1) and the matrix (N3) have a BCC crystal structure but with different lattice parameters. Moreover, two sets of diffraction spots, as indicated by the red arrow along the [111] and [100] zone axes, suggest that the Ta-Nb-rich precipitate has an orientation similar to the BCC matrix but with a slight tilt due to the lattice mismatch. The SAED patterns of the N2 area along the zone axes of $[01\bar{1}\bar{1}]$ and $[2\bar{1}\bar{1}0]$ are shown in Fig. 4(c, d), confirming a Hf-Zr-rich HCP phase. Fig. 4(e, f) presents the mixed diffraction patterns of the HCP phase and the BCC matrix. The crystallographic-orientation relationship between this HCP phase and the matrix is revealed as $\{0001\}_{hcp}//\{1\bar{1}0\}_{BCC}$ and $[2\bar{1}\bar{1}0]_{HCP}//[111]_{BCC}$, a classical Burgers orientation relationship (OR) [16].

The equilibrium mole fraction of stable phases as a function of temperature for the HfNbTaTiZr RHEA was calculated in [12], which predicts the formation of a single BCC solid-solution phase in a temperature range from 1020 to 1200 °C. At 1020 °C, another BCC phase enriched with Nb and Ta starts to precipitate, and an HCP phase mainly consisting

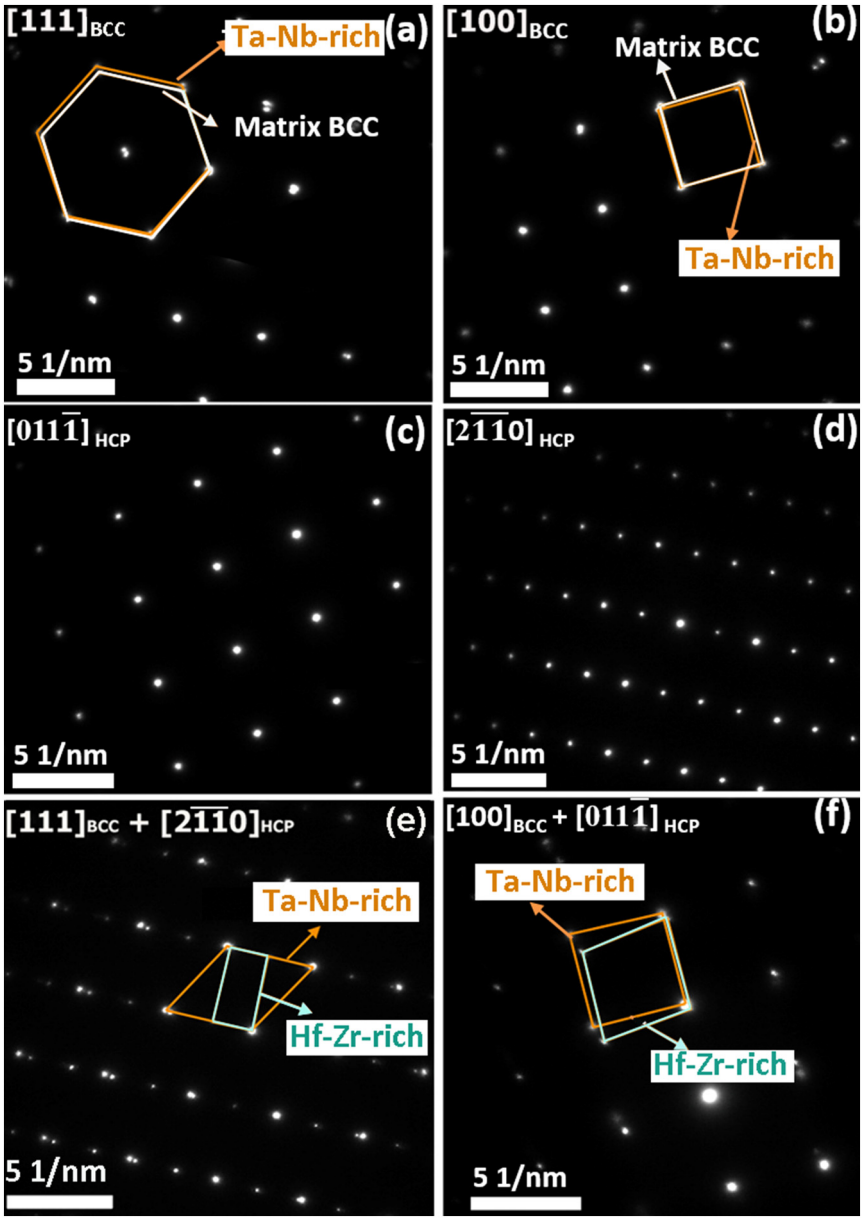

Fig. 4. SAED patterns from both BCC1 and BCC2 phases taken along the [111] (a) and [100] (b) zone axes (ZA) of the matrix; SAED patterns from the HCP phase taken from the $[01\bar{1}\bar{1}]$ (a) and $[2\bar{1}\bar{1}0]$ (b) ZAs; SAED patterns from both BCC1 and HCP phases taken along the [111] (a) and [100] (b) ZAs of the matrix.

of Hf, Ti, and Zr starts to form at 800 °C [12]. In other words, below 1020 °C, the single BCC phase is no longer thermodynamically stable and begins to decompose into a multi-phase structure. At 700 °C, the database predicts co-existing Ta-Nb-rich BCC and Hf-Zr-rich HCP phases. However, some disagreements exist between the CALPHAD calculations [12] and the present experiments at 550 and 700 °C. Calculations [12] predict that two phases co-exist at 550 and 700 °C. But the annealing experiment at 550 °C for 96 h presents that three phases co-exist and annealing at 700 °C for 96 h shows the formation of the HCP phase in a minor fraction. Note that the annealing time may be too short to reach the equilibrium state. In fact, Fig. 2(a) shows that the diffraction peaks from the residual BCC matrix at 550 °C become weak with only one major peak existing in the diffraction pattern. The calculation predicts very well for Ta, Ti, and Zr contents in the BCC phase and Ta, Nb, Zr, and Hf contents in the HCP phase, compared with experiments (Table 2), but the Nb and Hf contents in the BCC phase and Ti content in the HCP phase do not match the experimental result in both phases.

Even though most of the published literatures found a single BCC structure after the homogenization at high temperatures, the HfNbTaTiZr alloy exhibits phase decomposition when annealed in the intermediate temperature range [6,9–12]. It is known that the Nb and Ta elements possess a stable BCC structure in a wide range of temperatures, while Ti, Zr, and Hf manifest an HCP structure at low temperatures but a BCC structure at high temperatures [17]. To explain the anomalous phase decomposition in the HfNbTaTiZr alloys upon the post-heat treatment, the crystal structure of the constituent metal and the binary diagrams formed by the alloy's constituents should be considered. As suggested by the Ta-Nb phase diagram, a solid-solution alloy forms for all concentrations and maintains a BCC structure at both low and high temperatures, but the HCP structure is the low-temperature stable phase for Hf, Zr, and Ti, and their binary phase diagrams show a BCC-to-HCP phase transformation above a certain temperature. Thus, it is highly possible that an extra HCP phase is formed in the single-phase HfNbTaTiZr RHEA during the post-heat treatment process. Furthermore, in a recent study [12] of the annealing effect on the nanocrystalline HfNbTaTiZr RHEA made by high-pressure torsion, three phases were detected and confirmed as BCC1, BCC2, and HCP structure by synchrotron XRD. However, it is not the case in the present work. The decomposition found in the current work, which occurs during the annealing process at 700 °C, is from the as-quenched state obtained by water quenching after homogenizing at 1200 °C. This trend means that the effect of the cold-worked structure on free energies of different phases and thus the equilibrium state could be avoided in the present work. Therefore, the present experimental design could clearly reveal the evolution and the approach to the equilibrium state during annealing without the cold-worked structure effect.

The phase stability of the as-cast HEAs is often predicted, based on some widely-adopted empirical parameters, including the mixing enthalpy (ΔH_{mix}), mixing entropy (ΔS_{mix}), and atomic-size misfit (δ %) [18]. The empirical criteria for the formation of a single-phase BCC HEA are -15 kJ/mol $< \Delta H_{mix} < 5$ kJ/mol [19], valence electron concentration (VEC) < 6.87, and $1\% < \delta < 6\%$ [18,20]. Table 3 lists the VEC and atomic size for each composing element [21], and Table 4 presents the mixing enthalpy of all possible atomic pairs among the five constituents [22]. For the HfNbTaTiZr RHEA, VEC $= 4.4$, $\delta = 4\%$, and $\Delta H_{mix} = 2.72$ kJ/mol meet the criteria, which is consistent with the single-phase formation in the high-temperature range. However, this prediction is essentially for the phase equilibrium at high temperatures close to the melting point, where the mixing-entropy effect could be fully utilized to enhance the formation of solid solutions.

Table 3
The atomic size and VEC of composing elements.

Element	Ta	Nb	Ti	Zr	Hf
Atomic size (Å)	1.430	1.429	1.462	1.603	1.578
VEC	5	5	4	4	4

Table 4
The mixing enthalpies (kJ/mol) between composing elements in liquid state [22].

	Nb	Ti	Hf	Zr
Ta	0	1	3	3
Nb	0	2	4	4
Ti	–	0	0	0
Hf	–	–	0	0
Zr	–	–	–	0

As for the phase decomposition in the sample annealed at 700 °C, it can be thermodynamically explained with the decreased high-entropy effect, since some other factors would become significant, as compared to the decreased high-entropy effect at lower temperatures. In fact, the three criteria mentioned above relate with the chemical bonding, crystal-structure tendency, and atomic-size difference, respectively, and affect the Gibbs free energy. From the basic relation, $\Delta G_{mix} = \Delta H_{mix} - T\Delta S_{mix}$, for each kind of structure, ΔH_{mix} is actually the chemical-bonding-energy change, ΔH_{chem}, plus the strain-energy-induced ΔH_{strain}. "VEC" and "δ" relate with ΔH_{strain} [18] and these three factors basically do not change with temperature. The influence on the free energy for different temperatures can be regarded to be small, which means that the mixing entropy effect becomes the main factor as the temperature is a multiplier of entropy in the ΔG_{mix} equation. Under this condition, the free energy of the high-entropy solid solution is raised more rapidly, relative to competing low-entropy phases when temperature is lowered.

In conclusion, the crystal structure and microstructure of the homogenized HfNbTaTiZr alloy after annealing at intermediate temperatures (550 °C, 700 °C, 900 °C and 1000 °C) for 96 h or at 700 °C for 2.5 h, 96 h, and 192 h are systematically investigated. The TEM study of the crystal structure and composition reveals that the HfNbTaTiZr RHEA decomposes into three phases, the BCC matrix, BCC Ta-Nb-rich, and HCP Zr-Hf-rich precipitates when annealing at 700 °C even after a short-period of annealing time, 2.5 h. SAED study further unveils that both the BCC and HCP precipitates have preferred orientations with the BCC matrix, the orientation of the BCC precipitates is similar to the matrix but with a slight tilt due to large lattice mismatch and with an orientation relationship between the matrix and the HCP as $\{0001\}_{hcp}//\{1\bar{1}0\}_{BCC}$ and $[2\bar{1}\bar{1}0]_{HCP}//[111]_{BCC}$.

Acknowledgment

We are grateful for the support of the Department of Energy (DOE) Office of Fossil Energy, National Energy Technology Laboratory (NETL) (DE-FE-0011194) and the National Science Foundation (DMR-1611180 and 1809640), with Drs. J. Mullen, V. Cedro, R. Dunst, S. Markovich, G. Shiflet, and D. Farkas as program managers. R. F. and P.K.L. very much appreciate the support from the U.S. Army Office Project (W911NF-13-1-0438) with the program manager, Drs. M. P. Bakas, S. N. Mathaudhu, and D. M. Stepp. S.Y.C. and P.K.L. would like to acknowledge the financial support of the Center for Materials Processing (CMP), at The University of Tennessee, with the director of Dr. Claudia J. Rawn. M.C.G. acknowledges the support of the Cross-Cutting Technologies Program at the US DOE NETL under the RES contract of DE-FE0004000. The current research used resources of the National Energy Research Scientific Computing Center (NERSC), a U.S. Department of Energy Office of Science User Facility operated under Contract No. of DE-AC02-05CH11231. APT was conducted at ORNL's Center for Nanophase Materials Sciences (CNMS), which is a U.S. DOE Office of Science User Facility. The use of the Advanced Photon Source and Center for Nanoscale Materials at ANL, an Office of Science user facility, was supported by the U.S. Department of Energy, Office of Science, Office of Basic

Energy Sciences, under Contract No. of DE-AC02-06CH11357. J.W.Yeh would like to thank the financial support by the "High Entropy Materials Center" from The Featured Areas Research Center Program within the framework of the Higher Education Sprout Project by the Ministry of Education (MOE) and from the Project of MOST 107-3017-F-007-003 by the Ministry of Science and Technology (MOST) in Taiwan. XRD was performed at the Joint Institute for Advanced Materials (JIAM) Diffraction Facility, located at the University of Tennessee, Knoxville.

References

[1] O.N. Senkov, S.V. Senkov, C. Woodward, D.B. Miracle, Acta Mater. 61 (2012) 1545–1557.
[2] S.-P. Wang, J. Xu, Mater. Sci. Eng. C 73 (2016) 80–89.
[3] Y. Zhang, T.T. Zuo, Z. Tang, M.C. Gao, K.A. Dahmen, P.K. Liaw, Z.P. Lu, Prog. Mater. Sci. 61 (2014) 93.
[4] D.B. Miracle, O.N. Senkov, Acta Mater. 122((2017) 448–511.
[5] Y. Zhang, Y. Liu, Y. Li, X. Chen, H. Zhang, Mater. Lett. 174 (2016) 82–85.
[6] O.N. Senkov, J.M. Scott, F. Meisenkothen, S.V. Senkova, D.B. Miracle, C.F. Woodward, J. Mater. Sci. 47 (2012) 4062–4074.
[7] S. Vrtnik, P. Koželj, A. Meden, S. Maiti, W. Steurer, M. Feuerbacher, J. Dolinšek, J. Alloys Compd. 695 (2016) 3530–3540.
[8] A.D. Pogrebnjak, I.V. Yakushchenko, O.V. Bondar, O.V. Sobol, V.M. Beresnev, K. Oyoshi, H. Amekura, Y. Takeda, Tech. Phys. Lett. 41 (2015) 1054–1057.
[9] O.N. Senkov, S.L. Semiatin, J. Alloys Compd. 649 (2015) 1110–1123.
[10] O.N. Senkov, A.L. Pilchak, S.L. Semiatin, Metall. Mater. Trans. A 49 (7) (2018) 2876–2892.
[11] N.D. Stepanov, N.Y. Yurchenko, S.V. Zherebtsov, M.A. Tikhonovsky, G.A. Salishchev, Mater. Lett. 211 (2017) 87–90.
[12] B. Schuh, B. Völker, J. Todt, N. Schell, L. Perrière, J. Li, J.P. Couzinié, A. Hohenwarter, Acta Mater. 142 (2018) 201–212.
[13] A.P. Hammersley, S.O. Svensson, A. Thompson, H. Graafsma, Å. Kvick, J.P. Moy, Rev. Sci. Instrum. 66 (1995) 2729–2733 (SRI-94).
[14] W. Guo, D.A. Garfinkel, J.D. Tucker, D. Haley, G.A. Young, J.D. Poplawsky, Nanotechnology 27 (2016), 254004. .
[15] K. Thompson, D. Lawrence, D.J. Larson, J.D. Olson, T.F. Kelly, B. Gorman, Ultramicroscopy 107 (2007) 131–139.
[16] W.G. Burgers, Physica 1 (1934) 561–586.
[17] H. Okamoto, Desk Handbook: Phase Diagrams for Binary Alloys, ASM International, Materials Park, OH, 2000.
[18] Y. Zhang, Y.J. Zhou, J.P. Lin, G.L. Chen, P.K. Liaw, Adv. Eng. Mater. 10 (2007) 534–538.
[19] J.-W. Yeh, JOM 67 (2015) 2254–2261.
[20] S. Guo, C. Ng, J. Lu, C.T. Liu, J. Appl. Phys. 109 (2011), 103505. .
[21] S. Guo, C.T. Liu, Prog. Nat. Sci.: Mater. Int. 21 (2011) 433–446.
[22] A. Takeuchi, A. Inoue, Mater. Trans. 46 (2006) 2817–2829.